1 **A high-resolution pan-Arctic meltwater discharge dataset from**

2 **1950 to 2021**

3 Adam Igneczi[1*], Jonathan Bamber[1,2]

4 [1]Bristol Glaciology Centre, School of Geographical Sciences, University of Bristol, UK

5 [2]Department of Aerospace and Geodesy, Technical University of Munich, Germany

6 * *Correspondance: Ádám Ignéczi <a.igneczi@bristol.ac.uk, ignecziadam@gmail.com>*

7 **Abstract**

8 Arctic air temperatures have increased about four times faster than the global average since

9 about 1980. Consequently, the Greenland Ice Sheet has lost about twice as much ice as the

10 Antarctic Ice Sheet between 2003 and 2019, and mass loss from glaciers and ice caps is also

11 dominated by those that lie in the Arctic. Thus, Arctic land ice loss is currently a major

12 contributor to global sea level rise. This increasing freshwater flux into the Arctic and North

13 Atlantic oceans, will also impact physical, chemical and biological processes across a range of

14 domains and spatiotemporal scales. Although, meltwater discharge data at Arctic coastlines

15 are available from two existing datasets, these are limited by their spatial resolution and/or

16 coverage. Here, we extend previous work and provide a high-resolution coastal meltwater

17 discharge data product that covers all Arctic regions, where land ice is present, i.e. the

18 Canadian Arctic Archipelago, Greenland, Iceland, Svalbard, Russian Arctic Islands. Coastal

19 meltwater discharge data were derived from Modèle Atmosphérique Régional (MAR) daily

20 ice and land runoff products between 1950 and 2021, which we statistically downscaled from

21 their original ~6 km resolution to 250 m. The complete data processing algorithm, including

22 downscaling, is fully documented and relies on open-source software. The coastal discharge

23 database is disseminated in easily accessible and storage efficient netCDF files.

1. Introduction

Arctic air temperatures have increased about four times faster than the global average during the last four decades (Rantanen et al., 2022). One of the consequences of this is increasing land ice loss. The Greenland Ice Sheet (GrIS) has lost about twice as much mass as the Antarctic Ice Sheet between 2003 and 2019 (Smith et al., 2020, IPCC, 2021). Over the same period, glaciers and ice caps (GIC) in the Arctic – i.e. in Alaska, Canadian Arctic Archipelago, Iceland, Svalbard, Russian Arctic Islands – and peripheral GIC (PGIC) in Greenland were responsible for about 71% of the global GIC mass loss (Hugonnet et al., 2021). Altogether the GrIS and Arctic GIC lost a similar amount of ice during the last two decades. The rate of land ice loss has also been reported to have accelerated across the Arctic, except for Iceland (Ciracì et al., 2020), over the last few decades. Notably, mass loss rate in Greenland – i.e. the ice sheet and its PGICs – has been estimated to have increased sixfold between 1980 and 2020 (Mouginot et al., 2019). Due to these processes, Arctic land ice loss is currently a major contributor to global sea level rise (Frederikse et al., 2020; IPCC, 2021) and to the freshwater budget of the Arctic and North Atlantic oceans (Bamber et al, 2018).

Arctic GIC and the GrIS lose mass through a combination of decreasing surface mass balance – i.e. increasing surface runoff relative to precipitation – and increasing solid ice discharge (hereafter termed discharge). Although about two-thirds of the net mass loss from the GrIS between 1972-2018 is attributable to discharge (Mouginot et al., 2019), the relative contribution of this process has diminished to about 30-50% since 2000 due to increasing surface runoff (Enderlin et al., 2014; van den Broeke et al., 2016; Mouginot et al., 2019; King et al., 2020). This process plays an even more prominent role in land ice loss elsewhere in the Arctic; about 87% of the GIC mass loss between 2000 and 2017 across the Canadian Arctic Archipelago, Iceland, Svalbard, and the Russian Arctic Islands has been attributed to decreasing surface mass balance (Tepes et al., 2021). These trends illustrate the growing role of liquid meltwater discharge into Arctic seas, impacting physical, chemical and biological processes across a range of domains and spatiotemporal scales (Catania et al., 2020). Meltwater discharge at the ice-ocean interface of tidewater glaciers can also modulate discharge by influencing calving rates and ice dynamics (e.g.: Cowton et al., 2019; Melton et al., 2022). However, perhaps most importantly, increasing glacial freshwater flux – consisting of meltwater discharge and solid ice discharge – can influence the large-scale oceanic

circulation of the Arctic and sub-polar North Atlantic (SNA) Oceans (e.g.: Boning et al., 2016; Gillard et al., 2016; Yang et al., 2016; Dukhovskoy et al., 2019; Biastoch et al., 2021) and potentially the Arctic climate (Proshutinsky et al., 2015).

Despite its importance for a wide range of processes at varying spatiotemporal scales, only two studies provide data covering a multi-decadal time span over most, but not all, of Arctic land ice. These datasets rely on Regional Climate Model (RCM) runoff products – Modèle Atmosphérique Régional (MAR) and/or Regional Atmospheric Climate Model (RACMO) – digital elevation models, ice masks, statistical downscaling and meltwater routing algorithms to estimate coastal surface runoff fluxes. Bamber et al. (2018) utilise RACMO2.3p2 and RACMO2.3p1 products (1958-2016) – for the GrIS and GIC respectively – downscaled from 11 km to 1 km and cover most of the Arctic and Sub-polar North Atlantic (SNA) Oceans region with significant land ice presence, except for the Russian Arctic Islands. Although the coverage is fairly comprehensive, the data is reported at a relatively low spatial (5 km) and temporal (monthly) resolution. Mankoff et al., (2020) use both RACMO and MAR products (1950-2021) to provide high resolution data – daily, with modelled runoff inputs downscaled from 7.5 km (MAR) and 5.5 km (RACMO) to 1 km and routed by using a 100 m resolution DEM – but only for Greenland. Here, we attempt to combine the advantages of these two datasets, i.e. the high resolution of Mankoff et al. (2020) and the large coverage of Bamber et al (2018), and provide a high resolution (daily, downscaled to- and routed at 250 m) meltwater discharge dataset for the period of 1950-2021 in an easily accessible and storage efficient database that covers the most important land ice sectors of the Arctic and SNA Ocean regions, i.e. the Canadian Arctic Archipelago, Greenland, Iceland, Svalbard, Russian Arctic Islands.

2. An overview of the data processing pipeline

Our goal is to obtain a high resolution coastal meltwater discharge product that partitions meltwater according to its source, i.e. tundra, ice surface, and ice surface below the snowline (i.e. bare ice). To achieve this, we first downscaled coarse resolution (~ 6 km) RCM products: ice and tundra runoff, ice albedo; using their native vertical gradients and high resolution (250 m) surface DEMs (Figure 1). Downscaled ice albedo is only used to provide contextual information, i.e. to partition downscaled ice runoff according to its source (above or below the snowline). Limitations due to coarse resolution ice and land masks supplied with the RCM were addressed during this step by integrating high-resolution (250 m) ice and land masks into the downscaling algorithm (Figure 1). The high-resolution surface DEM that is used in the downscaling process is also used to delineate drainage basins and coastal outflow points in a hydrological routing algorithm. These drainage basins are used to sum the daily meltwater runoff and estimate meltwater discharge at the corresponding coastal outflow points (Figure 1). In order to limit computational requirements needed at any one time, we carried out the above process separately for each major glacier region. These are delineated according to the first order regions defined in in the Randolph Glacier Inventory v.6.0 (RGI Consortium, 2017): RGI-03 (Arctic Canada North), RGI-04 (Arctic Canada South), RGI-05 (Greenland), RGI-06 (Iceland), RGI-07 (Svalbard and Jan Mayen), RGI-09 (Russian Arctic) (Figure 2).
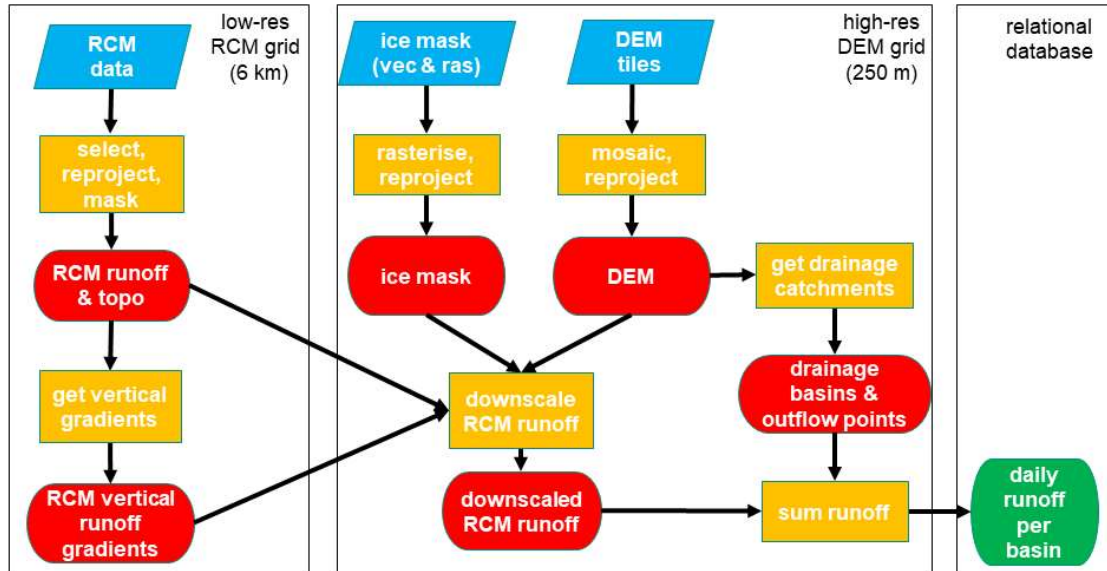
98 **Figure 1.** Data pipeline

99 ## 3. Input data pre-processing

100 ### 3.1. Static data

101 We assumed that time dependent changes in surface topography, land and ice
102 extent have negligible impact on large-scale surface runoff during our period of interest, i.e.
103 between 1950-2021. Hence we used static data products to obtain information about these
104 physical properties.

105 ### 3.1.1. DEM and land-ocean mask

106 High resolution (3"; ~90 m) DEMs were obtained from the Copernicus GLO-90 DGED
107 DEM product (ESA, 2021). This DEM is distributed in 1°x1° tiles and is referenced on the WGS-
108 84 ellipsoid. This product is in several ways superior to ArcticDEM – unless very high resolution
109 (i.e. up to 1 m) is required – as it is gapless and resolves small islands and coastal areas
110 precisely. ArcticDEM often has large elevation errors and significant data gaps close to coastal
111 areas and small islands (e.g. Mankoff et al., 2020). Water Body Mask (WBM) tiles are also
112 supplied with the GLO-90 DEM on the same grid. This provides a convenient way of separating
113 terrestrial and oceanic domains which are consistent with the DEM. We used this product to
114 create a binary land mask by selecting non-ocean pixels.

115   Using the RGI first order region outlines and the GLO-90 DEM grid shapefile we have
116   selected the required DEM and WBM tiles for each of the investigated RGI regions using the
117   open-source GIS software package QGIS. These tile lists, saved as text files, were used to
118   create DEM and WBM virtual mosaic files in the python geospatial library GDAL. After defining
119   the binary land-ocean masks from the WBM mosaics, we discarded DEM pixels coinciding
120   with the ocean mask to ensure we only retain valid DEM heights for terrestrial areas. The
121   mosaics were then reprojected in GDAL – using bilinear interpolation for DEM and nearest-
122   neighbour for WBM – to a 250 m grid referenced in an equal-area projected coordinate
123   system (North Pole Lambert Azimuthal Equal-Area Atlantic; EPSG:3574) to avoid the need for
124   scaling corrections further down the data pipeline due to area distortions (Snyder, 1987;
125   Bamber et al., 2018; Mankoff et al., 2020). Finally, the reprojected DEM and land-ocean mask
126   mosaics were clipped with the RGI region outlines. Henceforth we will refer to these products
127   as COP-250 DEM and COP-250 Land Mask. These products are also used further down the
128   data pipeline as reference grids for snapping.

129   **3.1.2. Ice mask**

130   As the RGI only provides glacier shapefiles for Greenlandic PGICs, we have used two
131   sources for our regional ice masks. Outside of Greenland we used RGI v.6.0 glacier outlines
132   (RGI Consortium, 2017). These are supplied in shapefiles referenced on the WGS-84 ellipsoid.
133   The shapefiles were first reprojected to EPSG:3574 and then rasterised to our reference 250
134   m grid (i.e. COP-250 DEM grid) using GDAL tools (ogr2ogr, gdal_rasterize) – a grid cell was
135   considered ice covered if its centroid was within RGI ice cover polygons. The COP-250 Land
136   Mask was then applied to correct for any potential mismatches (i.e. masking out oceanic
137   pixels) between the RGI and Copernicus datasets.

138   For the GrIS and Greenlandic PGICs we have used the GIMP v.1 ice mask product
139   (Howat et al., 2014; 2017). This is supplied as a mosaic for Greenland at a 90 m resolution grid
140   referenced in a polar stereographic projection system (NSIDC Sea Ice Polar Stereographic
141   North; EPSG:3413). After reprojecting it in GDAL – using nearest neighbour interpolation – to
142   the COP-250 DEM grid, which is using the equal area EPSG:3574 projected coordinate system,
143   we applied the COP-250 Land Mask to mask out potential oceanic pixels.

144   **3.2. RCM products**

145   Meltwater runoff and ice albedo both exhibit highly dynamic changes with time, thus

146   we obtained information on these properties from daily RCM outputs provided by MAR

147   v3.11.5 simulations (Fettweis et al., 2013, 2017; Maure et al., 2023) that were forced by 6

148   hourly ERA5 reanalysis data between 1950 and 2021. This product was chosen as it provides

149   data at relatively high spatial (~ 6 km) and temporal (daily) resolution for a large geographical

150   area, that almost completely covers our region of interest in the Arctic (Section 2). Altogether,

151   MAR data covers 6 Arctic RGI domains, though the MAR domain delineations do not follow

152   RGI conventions. Thus, MAR is distributed for 4 domains: Canadian Arctic (covering RGI-03

153   and RGI-04), Greenland (covering RGI-05), Iceland (covering RGI-06), and Russian Arctic and

154   Svalbard (covering RGI-07 and RGI-09) (Figure 2). Although the MAR domains only offer partial

155   coverage for some of their corresponding RGI regions, ice covered areas fall almost

156   completely within the MAR domains, with only a negligible amount of glaciers excluded

157   (Figure 2). However, a significant fraction of the tundra is not included in the RGI-03 (Arctic

158   Canada North) and RGI-04 (Arctic Canada South) and to a lesser degree in the RGI-09 (Russian

159   Arctic) regions (Figure 2). Thus, our data product cannot provide a full representation of the

160   tundra runoff in these RGI regions. Incomplete coverage was also taken into consideration

161   when delineating our drainage basins (Section 4.1) and when comparing our results with

162   previous studies (Section 5.4).

163
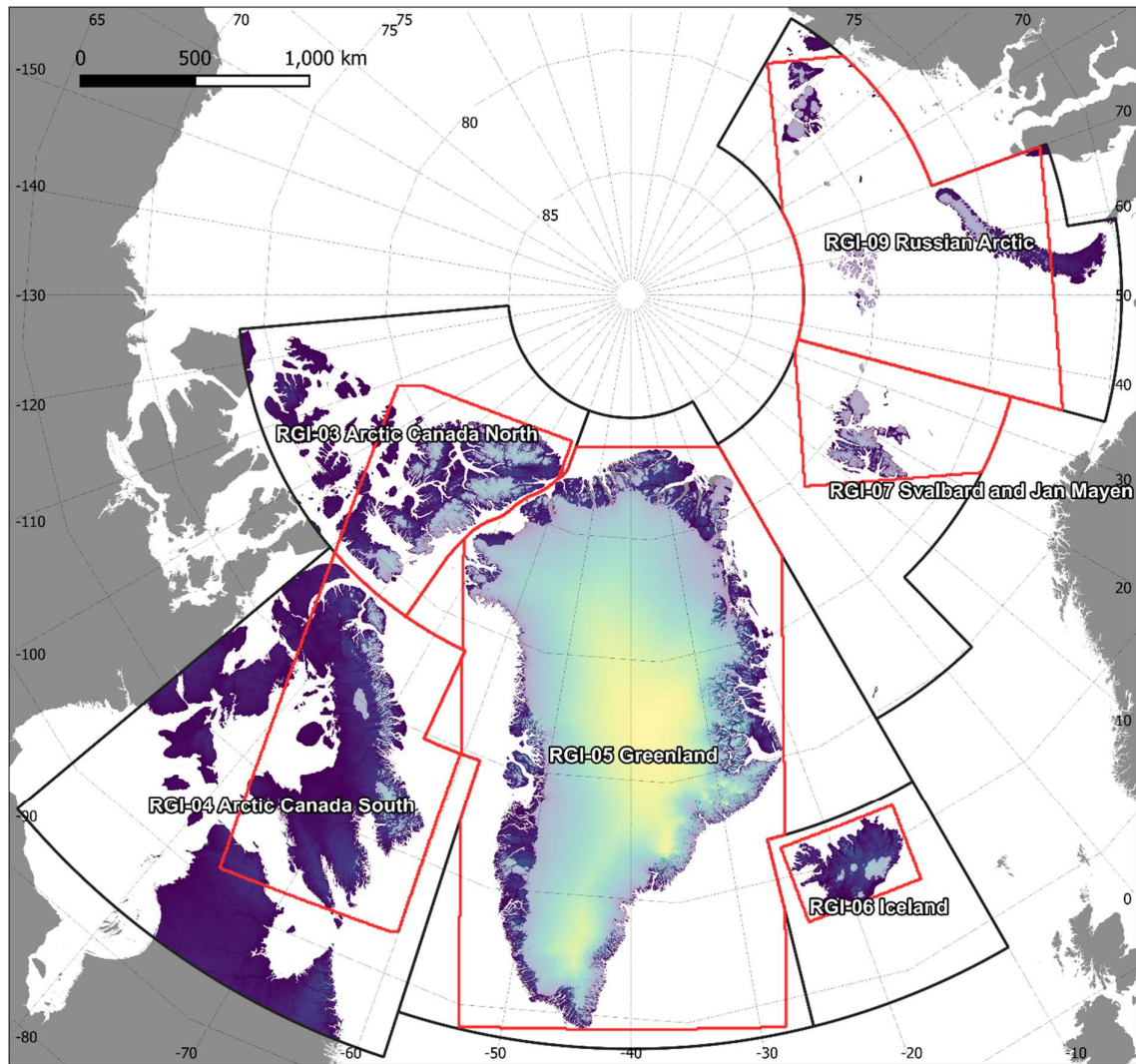
Figure 2. Overview map of our study area showing the COP-250 DEM with the ice coverage overlain (light shading). The investigated principal RGI regions (black line) and the MAR coverage (red line) are both displayed. MAR coverage plotted on the map has been clipped with the appropriate RGI region boundary.

MAR products are supplied in netCDF files, with each file holding a year's worth of daily data for a single MAR domain (i.e. there are 72 files for each of the 4 MAR domains). As the files contain many variables, we only extracted those we needed for our calculations (ice runoff, land/tundra runoff, ice albedo, surface elevation, and ice mask) to save computational time. Runoff, R, is defined as

$$R = ME + RA - RT - RF \text{ (Eq. 1)}$$

where ME is melt, RA is rainfall, RT is retention, and RF is refreezing. For tundra runoff RT and RF are both zero.

176   In lieu of a binary ice mask, this version of MAR introduces fractional ice coverage. Hence,

177   both land runoff and ice runoff data are provided for pixels with partial ice/tundra coverage.

178   The mask also contains generous fringe areas, where ice or tundra coverage is limited (< 0.001

179   %) and uniform. We simplified these fringe pixels by assuming them to be completely covered

180   by either ice or tundra. The corresponding ice or land runoff values were discarded (i.e. were

181   set to NoData), e.g. a pixel with 0.001% tundra coverage was assumed to be completely

182   covered by ice, thus the corresponding tundra runoff was discarded and ice runoff was

183   assumed to be valid for the whole pixel. This step reduced bias around ice-tundra boundaries,

184   e.g. during reprojection and resampling, and the calculation of vertical gradients.

185   MAR is referenced in a custom stereographic projection system, with a different set

186   of projection parameters for each domain. In addition, there is a 10° rotation for the Arctic

187   Canada domain, which needs to be reversed before reprojection. All MAR products were

188   reprojected from their custom system to EPSG:3574, while retaining their native 6 km

189   resolution. The reprojected MAR data were then clipped with the appropriate RGI region

190   boundary; this step also brings the MAR domains in line with the RGI regions thereby

191   consolidating our input data. During this step, we also saved the overlapping area between

192   the RGI regions and the MAR domains as shapefiles. This product is used further down the

193   processing pipeline to ensure that we are not extrapolating unreasonably beyond the spatial

194   coverage of valid MAR data. This issue, however, almost exclusively affects land runoff

195   products, as the ice covered regions within the investigated RGI regions are well captured by

196   MAR except for some small islands, e.g. Jan Mayen (Figure 2).

197   For computational efficiency, we have set up a parallel multiprocessing pool in

198   Python for each of the 6 investigated RGI region, with a dictionary ensuring that the

199   appropriate MAR domain is grabbed during processing. Then, we looped through the 72 years

200   covered by the MAR dataset and submitted each year separately to the pool as an

201   asynchronous task. Altogether 432 tasks were submitted, though the number of active

202   processes and pools were limited due to memory and core number constraints.

4. Methods

4.1. Drainage basins and outflow points

To obtain meltwater discharge volumes at Arctic coastlines, the RCM downscaling procedure needs to be combined with a hydrological routing scheme, which can use either the surface hydraulic head or the subglacial pressure head. In contrast to Mankoff et al. (2020), who assumed meltwater is immediately transported to the bed where it follows the subglacial pressure head, we have opted for a simpler approach and used surface routing exclusively. The principal reason for this is the lack of a pan-Arctic ice thickness product of sufficient accuracy and the relatively large uncertainty in bed topography even over the GrIS. Although, ice thickness estimates are available for all the RGI glaciers (Millan et al., 2022), this dataset is heavily reliant on shallow-ice approximation modelling and only covers Greenlandic PGICs and not the main ice sheet. The BedMachine product, which is based on mass conservation algorithms, is available for the latter region (Morlighem et al., 2017). However, ice thickness, especially for smaller glaciers outside Greenland, is highly uncertain compared to surface elevation. Furthermore, the aforementioned two datasets rely on fundamentally different methodology which would reduce the consistency of our input data.

The other source of uncertainty inherent to subglacial meltwater routing is due to the complexity of determining the exact timing, location and efficiency of surface-to-bed runoff capture. Although, it is well established that ice surface runoff can penetrate to the bed through ice of arbitrary thickness due to hydrofracturing (Das et al. 2008, Krawczynski et al., 2009), various factor influence this process, e.g. ice surface roughness, the pattern of surface fractures/crevasses, runoff volume, snow/firn thickness and saturation (Igneczi et al., 2018; Davison et al., 2019; Lu et al., 2021). Thus, meltwater can be routed for considerable distances on the ice surface before subglacial capture or proglacial discharge. Accordingly, supraglacial rivers exceeding several dozens of km-s in length, with some terminating at the ice margin, have been observed on the Devon and Barnes Ice Caps and in northern Greenland (Yang et al., 2019; Zhang et al., 2023). Connected to this issue, subglacial pressure head calculations usually assume that subglacial water pressure always equals the ice overburden pressure, i.e. the flotation-factor is constantly 1 (e.g. Mankoff et al., 2020). However, this assumption also introduces uncertainties as it disregards the spatiotemporal evolution of the subglacial drainage system (Davison et al., 2019).

234
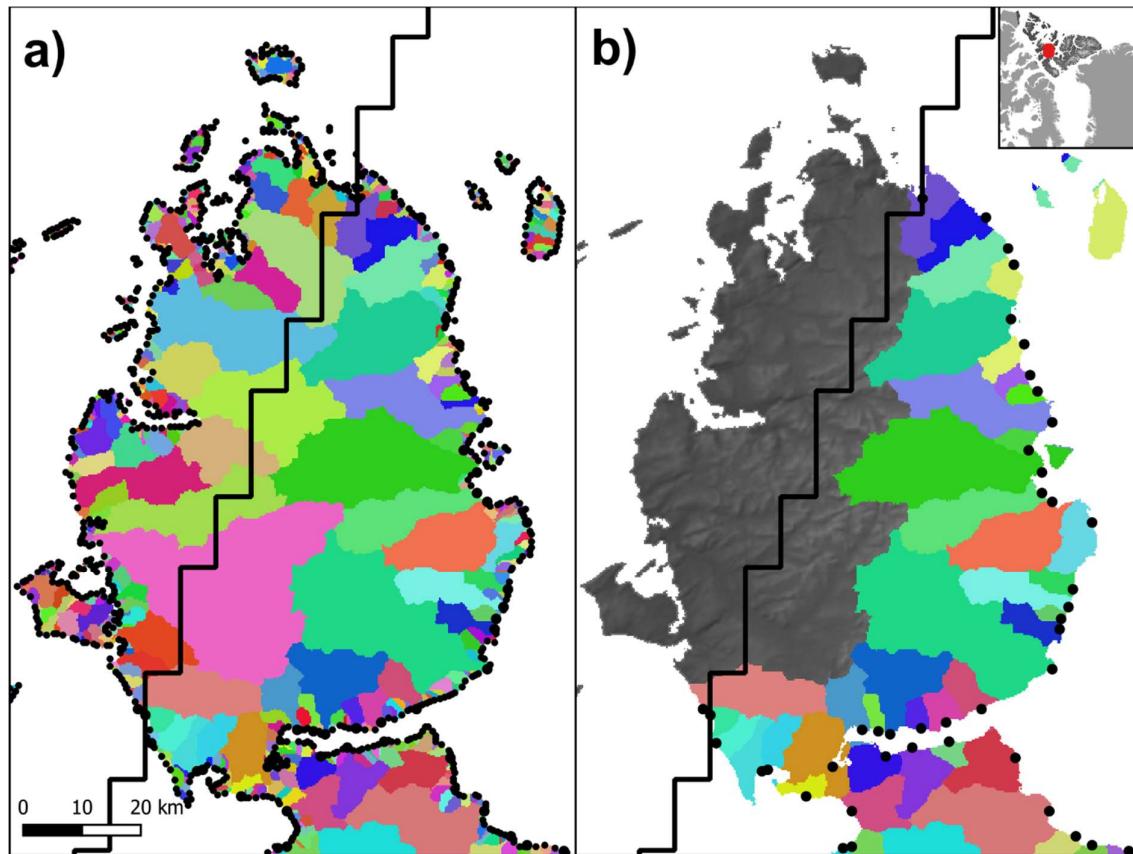
Figure 3. Surface drainage basins and their outflow points (black points) in Northern Canada (a) before and (b) after the removal of small basins and basins that have at least 90% of their area outside the MAR domain (solid black line).

In order to avoid these pitfalls and simplify our approach we used the previously created COP-250 DEM product (Section 3.1.1) to calculate surface drainage basins. These drainage basins were subsequently used to integrate the downscaled daily surface runoff following the approach of Mankoff et al., (2020). The workflow is fully automated by using the Whitebox tools (WBT) package in a Python script. After filling closed depressions and treating flat areas – to ensure these have an outflow point – in the COP-250 DEM with the *wbt.fill_depressions* tool (with the fix_flats option checked true), single D8 flow directions were calculated using *wbt.d8_pointer*. Then, distinct drainage basins were derived from the flow directions raster using the *wbt.basins* tool. The resulting product is an integer raster, with unique integers indicating basin coverage (Figure 3). In order to limit the number of basins, thereby aggregating our end product, we removed small basins (< 10 km^2) and set their corresponding pixels to NoData. Then, we allocated these pixels to their nearest valid basin using the *wbt.euclidean_allocation* tool (Figure 3). As this tool also assigns oceanic

251 pixels, we introduced an additional step to mask out the ocean. We also removed basins that
252 are touching the RGI region outline, buffered with the resolution of the COP-250 DEM. This
253 step ensures that all the drainage basins fall completely within the RGI domain. Data gaps in
254 the RCM products are filled in during the downscaling procedure to facilitate complete spatial
255 coverage (Section 4.3). However, to limit unreasonable spatial extrapolation, we only retained
256 surface drainage basins that have at least 90% of their area within the MAR domain (Figure
257 3).

258   Outflow points of the basins were calculated by finding pixels that have no flow
259 direction, i.e. no lower neighbours. These pixels were then converted to vector points and
260 saved to a shapefile. As the COP-250 DEM has previously been treated with the
261 *wbt.fill_depressions* tool with the fix_flat option – which ensures there are no closed
262 depressions and flat areas without outflow points, i.e. all pixels have a lower neighbour apart
263 from the edge pixels – these points will represent actual outflow points at the edges of the
264 basins. However, this step also yields the outflow point of basins that have been removed due
265 to their size or coverage (Figure 3). We have sampled the intermediate basin rasters to
266 identify and remove the outflow points that correspond to these removed basins. Thus, the
267 final product has a single outflow point for each valid basin, which is the outflow point
268 associated with the principal basin where fragments from smaller basins are included (Figure
269 3).

4.2. Vertical gradients of runoff and ice albedo

271   Localised regression analysis between elevation and modelled climatic parameters
272 has been used in various studies to statistically downscale reanalysis temperatures (e.g.:
273 Hanna et al., 2005; 2008; 2011; Gao et al., 2012; 2017; Dutra et al., 2020) and RCM estimates
274 of SMB components (e.g.: Franco et al., 2012; Noël et al., 2016, Tedesco et al., 2023). The
275 procedure of Franco et al., (2012) – downscaling MAR from 25 km to 15 km – relied on
276 localised vertical gradients that were obtained by calculating differences in elevation and
277 MAR variables within an 8-N moving window. They also applied vertical weighing, i.e.
278 averaged the vertical gradients by the total elevation difference within the kernel, to dampen
279 the influence of "extreme" local gradients. Noël et al. (2016) combined elevation dependent
280 downscaling – relying on localised linear regressions within a moving window – with empirical
281 accumulation, ablation, and bare ice albedo corrections. Tedesco et al., (2023) relied solely

282   on elevation dependent downscaling, which was carried out in a similar manner to Noël et al.

283   (2016) though SMB mass conservation was enforced within each original MAR pixel. They also

284   deployed a novel computational setup that achieved high efficiency and speed by strongly

285   leveraging parallelisation, which was enabled by highly segmenting the input data.

286   All these studies – at their core – rely on the inherent localised vertical lapse rates of

287   RCM products. Thus, we have adopted a similar approach that utilises these lapse rates to

288   statistically downscale daily MAR products from their native resolution of ~6 km to the 250 m

289   resolution COP-250 DEM grid. The setup of our downscaling procedure is based on Franco et

290   al. (2012) due to its relative simplicity, i.e. relying on differences within the moving window

291   instead of linear regression. However, the elevation dependent downscaling carried out by

292   Noël et al. (2016) and Tedesco et al. (2023) is also similar – except for their use of linear

293   regression, additional empirical corrections, and mass conservation enforcement.

294   To calculate the required vertical gradients, first, an 8-neighbourhood moving

295   window was applied to calculate the difference in elevation (i.e. the native DEM in MAR), ice

296   runoff, land runoff, and ice albedo – the latter for contextual purposes – between each pixel

297   and their 8 neighbours. Ice and land runoff were handled separately. Then, 8D local vertical

298   gradients were determined within the kernel by dividing ice runoff, land runoff, and ice albedo

299   differences with their corresponding elevation differences (Franco et al., 2012). NoData was

300   assigned to the centre of the kernel and 0 was assigned to every direction where the elevation

301   difference is below 50 m, the latter step corrects for bias caused by elevation independent

302   runoff and albedo variance. This step is a substitute for vertical weighing (Franco et al., 2012)

303   as it allows us to filter out elevation independent variance more completely and precisely.

304   To yield local vertical gradient rasters, the average of the kernel gradients was

305   assigned to each central pixel if at least 5 valid gradients were found within the kernel.

306   Otherwise, the central pixel was assigned NoData. In lieu of carrying out our own sensitivity

307   analysis, we relied on the conclusions of Noël et al. (2016) who ascertained that using 6

308   regressions points – i.e. equivalent to 5 valid gradients – provides the best balance between

309   converging to, or diverging from the low resolution RCM runoff products. Positive vertical

310   gradients in ice/land runoff (i.e. runoff increasing with elevation) and negative vertical

311   gradients in ice albedo (i.e. ice albedo decreasing with elevation) were discarded, i.e. assigned

312   NoData. Data gaps were filled in using bilinear interpolation inside the convex hull of valid

313   data, and nearest neighbour extrapolation outside of it.

314
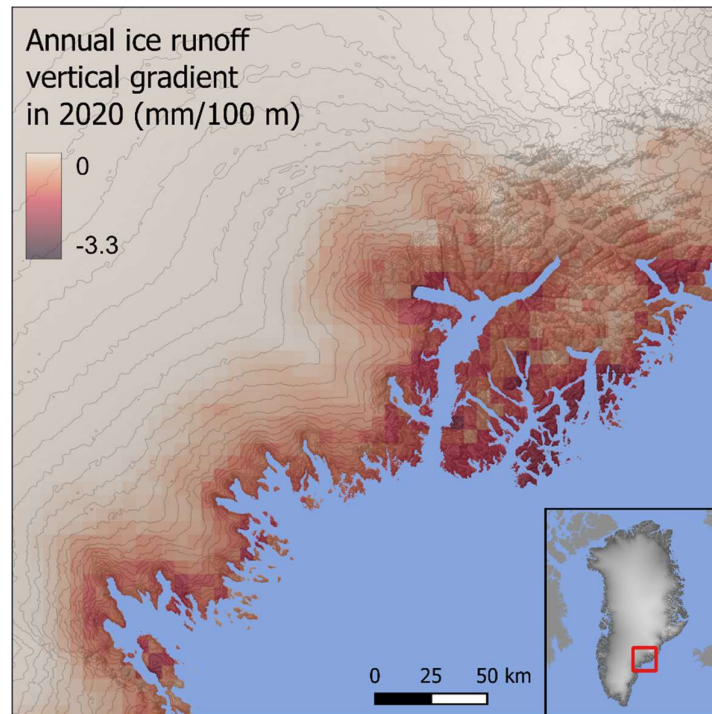
Figure 4. Annual average vertical ice runoff gradient for 2020 in SE Greenland; elevation contours are drawn every 100 m. The annual average is calculated from the daily vertical ice runoff gradients. Units are in mm/100 m, i.e. showing how many mm-s runoff will change with every 100 m elevation gain.

319   To accurately track the temporal evolution of the vertical gradients, we sequentially

320   looped through each day covered by the MAR products. Thus, the process was carried out

321   26,298 times for each of the 6 RGI domains, producing 473,364 rasters with 6km resolution.

322   Annual time-averaged vertical gradients were also produced and saved to GeoTiffs for

323   reference (Figure 4). To save computational time, the task was integrated with the script that

324   carries out MAR pre-processing (Section 3.2). This design, in addition to taking advantage of

325   an already existing parallel processing scheme, facilitated efficient I/O operations by writing

326   pre-processed (i.e. filtered, reprojected, clipped) MAR products and their derived localised

327   vertical gradients to the same file – RGI domain specific yearly netCDF files – at the same time.

328   Although parallelisation was not leveraged as effectively as by Tedesco et al. (2023), the task

329   completed pan-Arctic pre-processing in about a day.

4.3. Statistically downscaled runoff and ice albedo

331   The first step of the statistical downscaling algorithm was upsampling the pre-

332   processed MAR ice, and tundra runoff, ice albedo (Section 3.2), their vertical gradients

333   (Section 4.2), and the MAR DEM from their native resolution of ~6 km to the 250 m resolution

334   COP-250 DEM grid. Nearest neighbour interpolation was first applied to fill in data gaps, then

335   upsampling to the COP-250 DEM grid was carried out by bilinear interpolation (Figure 5, 6,

336   S1). Once all products were upsampled to the COP-250 DEM grid, elevation differences were

337   calculated between the MAR DEM and the COP-250 DEM (Figure 5, 6, S1). Elevation

338   corrections were then made by multiplying the elevation difference with the appropriate

339   localised vertical gradient raster and adding this to the upsampled ice, and tundra runoff and

340   ice albedo rasters (Franco et al., 2012). Ice and tundra runoff were handled separately.

341   Henceforth we refer to these rasters as the downscaled products. Oceanic pixels were masked

342   out from all of the downscaled rasters by using the high-resolution COP-250 Land Mask; while

343   ice and tundra runoff were masked by the appropriate high-resolution RGI or GIMP ice mask

344   (Figure 5, 6, S1). Pixels with negative runoff were assigned zero.

345   The downscaling procedure was carried out on the pre-processed daily MAR data,

346   which includes vertical gradients (Section 4.2). Although this procedure was handled

347   separately from MAR preprocessing, the computational setup is similar. A parallel

348   multiprocessing pool was created for each RGI region, then each task running asynchronously

349   on these pools grabbed a single year of data from the appropriate RGI region for processing.

350   Archiving downscaled daily runoff data – which have 250 m spatial resolution – would require

351   excessive storage capacity. To circumvent this problem, we only retained downscaled daily

352   runoff that was summed for the drainage basins. Thus, the algorithm, handling the integration

353   of runoff for the drainage basins (Section 4.4.), was combined with the downscaling

354   procedure. Annual runoff was also obtained for reference by summing the downscaled daily

355   products; these annual rasters were saved to GeoTiffs.

356
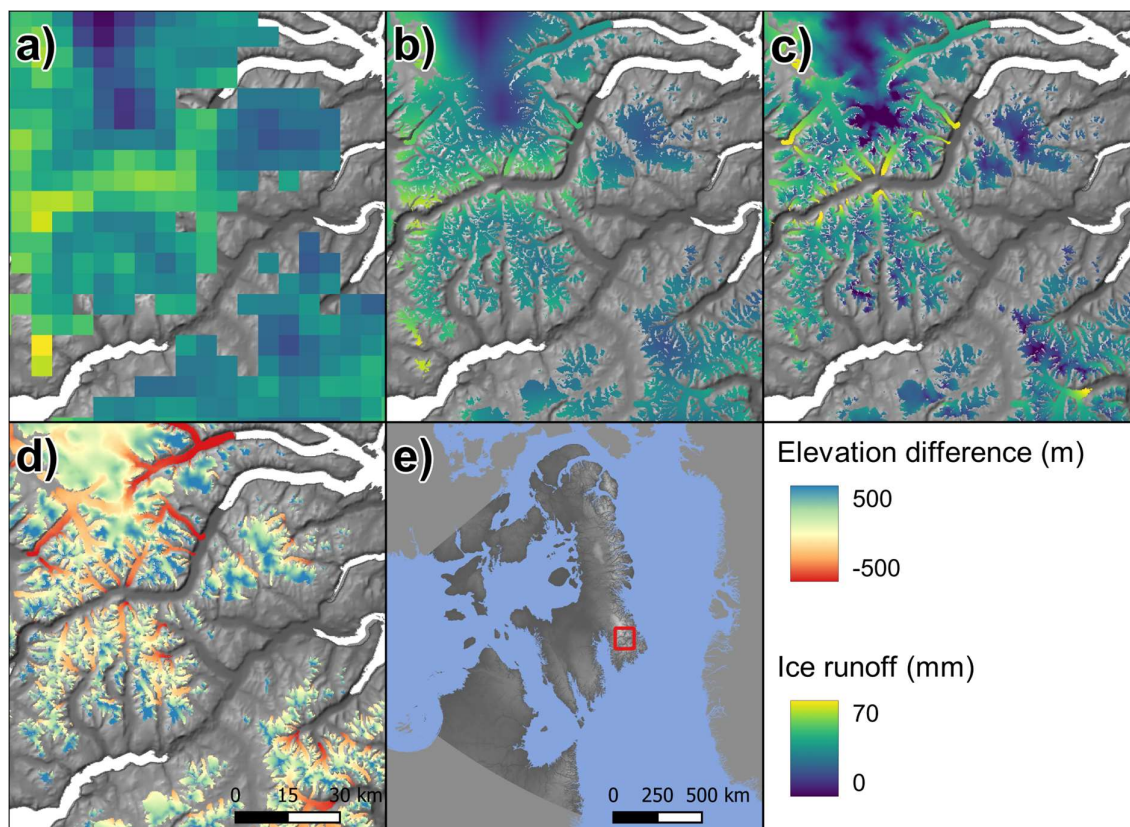
357 **Figure 5.** (a) Native resolution daily cumulative ice runoff for 19/July/2021 in Arctic Canada
358 South from MAR, runoff is plotted for fractional ice pixels; (b) ice runoff after upsampling to
359 250 m; (c) ice runoff after elevation correction, i.e. downscaling. (d) COP-250 DEM minus the
360 upsampled MAR DEM within the RGI ice mask. (e) Overview map.
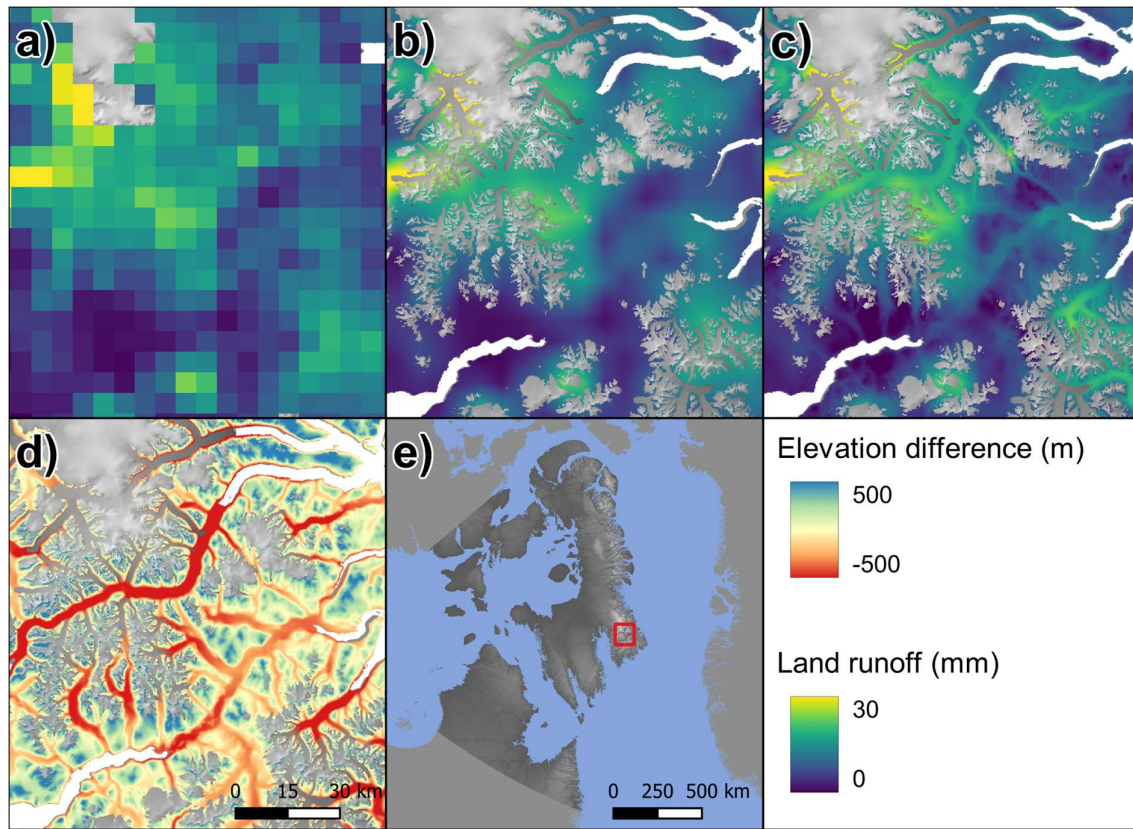
Figure 6. (a) Native resolution daily cumulative tundra runoff for 19/July/2021 in Arctic Canada South from MAR, runoff is plotted for fractional tundra pixels; (b) tundra runoff after upsampling to 250 m; (c) tundra runoff after elevation correction, i.e. downscaling. (d) COP-250 DEM minus the upsampled MAR DEM outside the RGI ice mask. (e) Overview map.

Although our statistical downscaling procedure is similar to the one that was applied on the input data of Mankoff et al. (2020), there are several key methodological differences. Mankoff et al. (2020) used RCM products that have been downscaled to 1 km resolution – following the procedure of Noël et al. (2016) – prior to their data processing, i.e. statistical downscaling was not integrated into their routing algorithm. As the two procedures were separate, the resolution of their routing products (100 m) do not align with the resolution of their downscaled RCM products (1 km), and ice domains do not overlap precisely. To alleviate these spatial discrepancies, Mankoff et al. (2020) scaled and snapped RCM products to the routing resolution. Pixels with mismatching domain types (e.g. land according to RCM but ice according to the routing product) were assigned the average runoff of the corresponding ice/land basin. No runoff was reported for small basins with no RCM coverage of the same type. As we carried out both the downscaling and the routing on the same grid, similar adjustments were not needed in our data processing algorithm.

4.4. Meltwater discharge at outflow points

After downscaling, daily ice and land runoff was summed over each drainage basin. In addition to carrying out this step for whole drainage basins, we also summed ice runoff separately for subsections of the basins where the ice albedo was below 0.7. As this is the minimum allowed albedo for the snow model in MAR (Fettweis et al., 2017), we propose that runoff originating from these regions is a good approximation for runoff from below the snow line (BSL). The reason for making this distinction is that, runoff above the snow line will be predominantly due to melt of seasonal snow, while runoff BSL is predominantly ice and firn melt and therefore a reduction in the "ice reservoir". This is an approximation but may be useful for investigating secular versus seasonal fluxes. However, it is important to note that MAR is known to overestimate bare ice areas, thus true snowline elevations might be lower than estimated here (Ryan et al., 2019; Fettweis et al.., 2020).
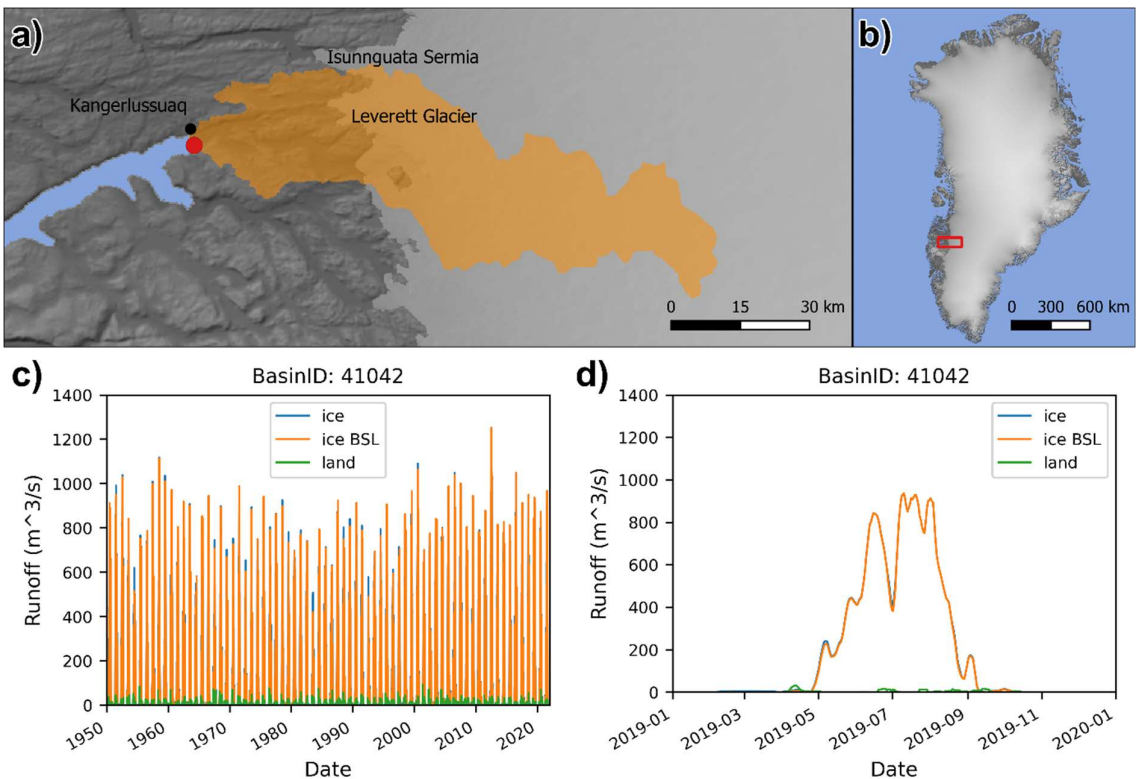
Figure 7. An example of our basin specific daily runoff data. (a) Coverage of the drainage basin, which includes Leverett and Russel Glaciers in West Greenland, and its coastal outflow point, (b) overview map. (c) Seven-day running average of the coastal meltwater discharge from ice, land and bare ice – i.e. ice below snow line (BSL) – runoff between 1950 and 2021, (d) zoomed in view of the same graph between 2019 and 2020.

397   The resulting basin specific daily runoff time-series were saved into three separate
398   tables – representing land, ice and bare ice runoff (Figure 7) – where rows represent days and
399   columns represent drainage basins. Due to the computational setup (Section 4.3), these
400   tables were initially saved to yearly RGI domain specific netCDF files. Thus, the final step was
401   concatenating these yearly files, to yield a single netCDF file for each RGI region which
402   contains the daily runoff data for each drainage basin within the region.

403   **5. Product evaluation**

404   **5.1. Validation against river discharge measurements**

405   To validate our product, we compared daily river discharge measurements from 7
406   locations in Greenland (Hawkings et al., 2016a, 2016b; Langley 2020; Sugiyama et al., 2014;
407   Kondo and Sugiyama 2020; van As et al., 2018) with our corresponding coastal meltwater
408   discharge time series, using the code published by Mankoff et al. (2020) for bulk comparisons.
409   Although river gauge data is available for 3 additional locations (Mankoff et al., 2020), we
410   were not able to integrate these with our product due to compatibility issues. Leverett Glacier
411   had to be removed as we only produce meltwater discharge time series at the coastlines, and
412   not at the glacier margins as in Mankoff et al. (2020). The four Greenland Ecosystem
413   Monitoring (GEM) river gauges near Nuuk – Kobbefjord, Oriartorfik, Kingigtorssuaq,
414   Teqinngalip – correspond to very small drainage basins, ranging from 7.56 to 37.52 km^2. Our
415   aggregation procedure – i.e. the merging of small basins (< 10 km^2) with their neighbours
416   (Section 4.1) – heavily affected these basins, thus direct comparisons with our products are
417   not possible. However, by investigating the topography and the non-aggregated basins of
418   Mankoff et al. (2020), we concluded that the neighbouring Kobbefjord and Oriartorfik gauges
419   – together – can reasonably represent discharge from the single aggregated basin that
420   contains them. Conversely, the Kingigtorssuaq and Teqinngalip gauges had to be completely
421   excluded as they only represent a small subsection of the aggregated basin that contains them
422   (Figure S2).

423
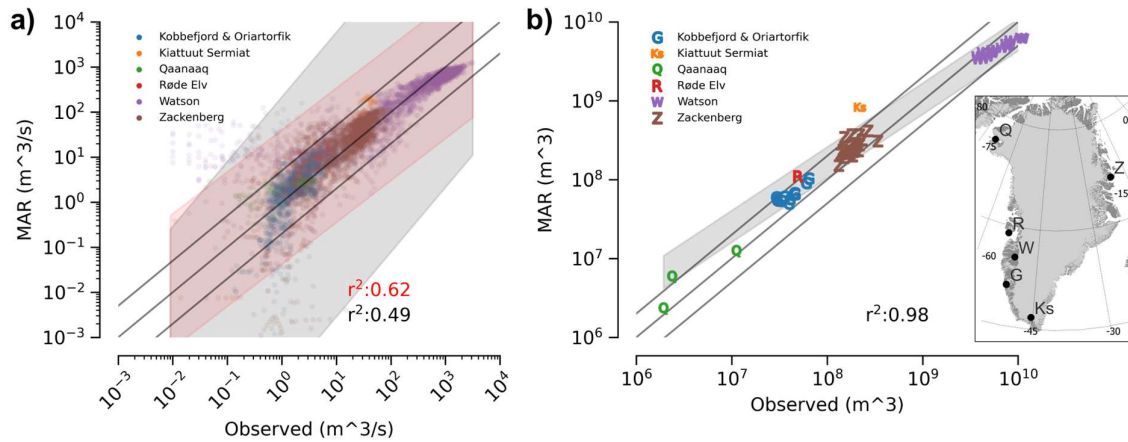
Figure 8. Bulk comparison of observed river gauge data and discharge derived from downscaled MAR. The map inset shows the location of the river gauges. Solid lines show 1:1 (centre), 1:5 (upper), and 5:1 (lower) correspondence. (a) Besides the original daily data, (b) annual sums calculated for calendar years are also compared. Grey band shows 5 % to 95 % prediction interval. Red band shows the same, when excluding the summed Kobbefjord & Oriartorfik data. Drawn by utilising code from Mankoff et al. (2020).

Overall, the performance of our dataset against field measurements is very similar to the performance reported by Mankoff et al., (2020) for their MAR based discharge estimations. Both the r^2 values – 0.45, and 0.59 when excluding the four GEM gauges near Nuuk – and the 5% to 95% prediction intervals reported by Mankoff et al. (2020) agree well with our results in the case of the daily data (Figure 8a). Annual results – i.e. daily discharge summed by calendar year for the days when observations exist – also exhibit similar performance with the r^2 (0.96) reported by Mankoff et al. (2020) (Figure 8b). However, our 5% to 95% prediction interval is slightly different. While the range is similar, it indicates that our dataset overestimates discharge towards the lower end of the annual discharge range. This is not surprising as we provide an aggregated product, i.e. very small basins are merged with their neighbours. The relative effect of the aggregation on discharge fidelity increases with decreasing basin size, which limits the feasibility of using our dataset for very small individual meltwater discharge outlets. However, it is important to note that bulk meltwater discharge is unaffected by this. Thus, we think the benefits of providing an aggregated product outweigh the limitations.

5.2. Comparison of downscaled and original MAR runoff

To reveal the specific effects of the downscaling procedure on our data product, we compared bulk downscaled runoff with the original MAR runoff, separately for the ice and

448 tundra domains of each RGI region (Figure 9). Downscaled runoff – when compared to the

449 original MAR runoff – exhibits an over- or underestimation that is characteristic to each RGI

450 region and is largely independent of the runoff amount, i.e. varies little year-to-year (Figure

451 9). This suggests that the factors that determine the effect of downscaling on our runoff

452 products are relatively static, and inherent to the investigated regions. In general, downscaled

453 ice runoff tends to underestimate the original MAR runoff (Figure 9, Table 1). This effect is

454 the strongest in Arctic Canada South and North (-23.5% and -12.5% respectively), elsewhere

455 it remains moderate (between -4.4% and -9%), while in Greenland there is a slight

456 overestimation (+2.4%). On the other hand, downscaled tundra runoff overestimates the

457 original MAR runoff in all the investigated regions. This is the most significant in Svalbard

458 (+28%), elsewhere it remains more moderate (< 12.6%).

459
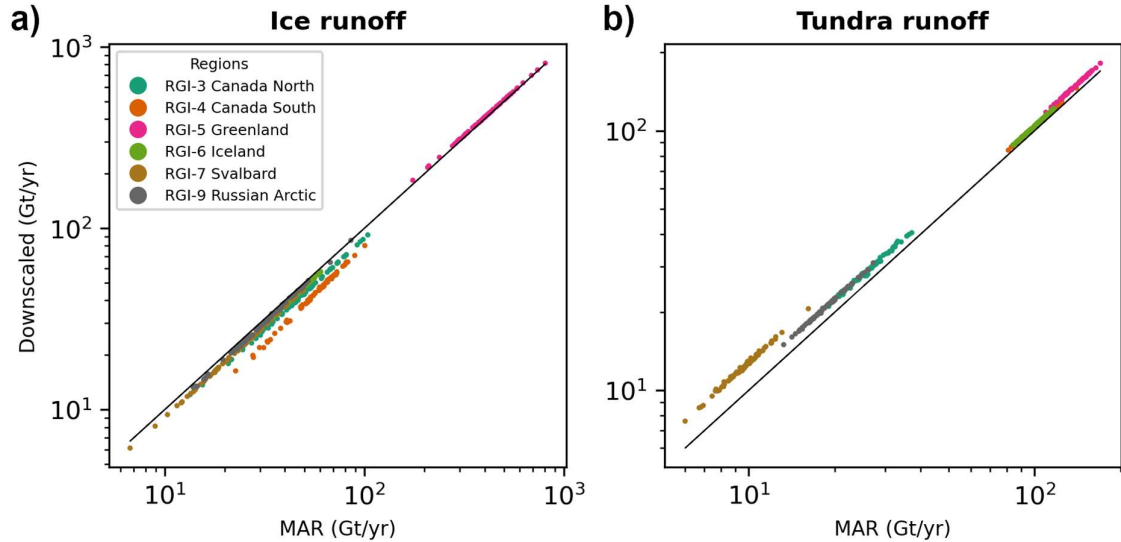
460 **Figure 9.** Annual sums of the original MAR runoff and the downscaled runoff, plotted
461 separately for (a) ice and (land) areas of the investigated RGI regions.

462   A significant amount of the MAR ice runoff underestimation can be attributed to the

463 reduction in ice area during the downscaling procedure, due to the differences between the

464 MAR and high-resolution ice masks (Table 1). However, this is not the only factor – e.g. in

465 Greenland ice areas largely match, while ice area increases during downscaling in the Russian

466 Arctic (Table 1). Thus, topography, especially the difference between MAR and high-

467 resolution DEMs, also need to be considered. In general, the COP-250 DEM is lower than the

468 MAR DEM within confined valleys, and higher along ridges, small plateaus, and peaks; flat

469 areas generally align well (Figure 5, 6, S3). If marine-terminating outlet glaciers – that drain

ice from a flat interior all the way to the sea – dominate the glaciated landscape, then elevations are generally overestimated by MAR (Figure S4), and runoff will increase with downscaling. This effect has been pointed out for Greenland by several studies (e.g.: Bamber et al., 2001; Noël et al., 2016) and our results also align with it. However, if valley glaciers – which might terminate at higher elevations – smaller ice caps, and plateau glaciers dominate the landscape, then elevations are generally underestimated by MAR (Figure S4), and runoff will decrease with downscaling. This effect – along with the reduction in ice area – can reasonably explain why downscaling underestimates MAR ice runoff in Arctic areas outside Greenland.

	Runoff RMSD	Runoff NRMSD (%)	Runoff average relative difference (%)	Area relative difference (%)
Ice				
RGI-3 Canada North	6.5	13.3	-12.5	-7.7
RGI-4 Canada South	13.3	23.4	-23.5	-16.6
RGI-5 Greenland	9.3	2.2	2.4	-0.03
RGI-6 Iceland	2.4	5.5	-5.5	-5.0
RGI-7 Svalbard	2.2	9.1	-8.7	-6.9
RGI-9 Russian Arctic	1.3	4.2	-4.4	3.7
Tundra				
RGI-3 Canada North	2.9	10.9	10.8	4.4
RGI-4 Canada South	4.3	4.2	4.2	1.6
RGI-5 Greenland	10.1	7.3	7.3	-0.4
RGI-6 Iceland	4.4	4.4	4.4	0.2
RGI-7 Svalbard	2.7	28.4	28.0	8.9
RGI-9 Russian Arctic	2.4	12.7	12.6	-3.6

Table 1. Root Mean Squared Deviation (RMSD) was computed comparing the annual sums of the original and downscaled runoff, normalising (NRMSD) was carried by the annual sum of the original runoff. The average difference (downscaled minus original) was also normalised by the original MAR runoff. The difference in the domain area (high-resolution mask minus MAR mask) is also provided relative to the MAR domain area.

MAR tundra runoff overestimation – to a smaller degree – can also be attributed to the reduction in ice area and the corresponding increase in land area during the downscaling procedure (Table 1). However, this relationship is not reciprocal as land area is also strongly influenced by the COP-250 Land Mask and by the removal of some edge basins (Section 4.1), generally the increase in land area is smaller than the decrease in ice area (Table 1). Thus, the net effect of topography is stronger on our downscaled tundra runoff than on the ice runoff. In mountainous regions of the Arctic, tundra is typically situated at lower elevations, e.g. the

491   lower, non-glaciated sections of valleys – as the upper section of valleys, higher ridges and

492   plateaus are mostly glaciated. Thus, tundra elevations are often overestimated by MAR,

493   where confined valleys with non-glaciated lower sections are abundant, e.g. in West Svalbard

494   and South Novaya Zemlya (Figure S3, S5). Runoff will increase with downscaling in such

495   situations, which provides a good explanation for the observed overestimation of MAR tundra

496   runoff (Figure 9). However, further studies might be needed to fully uncover the combined

497   effect of such static factors and the complex spatiotemporal evolution of melting on

498   downscaling products.

499   5.3. Comparison with previous work

500   We also carried out bulk comparisons between our downscaled ice and tundra runoff

501   products and the equivalent datasets from Bamber et al. (2018) and Mankoff et al (2020).

502   Bamber et al. (2018) provide data for most of the Arctic (but less complete than here).

503   Conversely, the study of Mankoff et al. (2020) is restricted to Greenland. Thus, two sets of

504   comparisons were performed, one for Greenland and one for the rest of the Arctic. Runoff

505   products computed for the Russian Arctic were excluded from these comparisons, as this

506   region has not been investigated by either of the aforementioned two studies. As our MAR

507   domains – and thus our meltwater discharge dataset – only partially cover some RGI regions,

508   especially in Arctic Canada (Figure 2), and Bamber et al. (2018) provides more complete

509   coverage of the RGI domains, we clipped the Bamber et al. (2018) dataset with our MAR

510   domains (Figure 2). These steps ensured that the compared datasets have similar scope and

511   coverage.

512   Bulk ice runoff for Greenland agrees well between the three datasets. Although, the

513   1σ intervals of the three datasets – when comparing 5-year running means and standard

514   deviations – overlap well (Figure 10a), we estimated slightly larger runoff than the other two

515   datasets. The mean difference between our bulk ice runoff and that of Bamber et al. (2018)

516   and Mankoff et al. (2020) – when comparing datasets before applying running means – is

517   +17.7 Gt and +27.9 Gt (equivalent to +5.1 and +7.3% increase), respectively. Our estimation

518   for bulk ice runoff from glaciers and ice caps in other Arctic regions outside of Greenland

519   differs to a greater degree from the dataset of Bamber et al. (2018), i.e. with a mean

520   difference of +38.3 Gt (+40.1%) (Figure 10c). As bulk ice runoff only increases slightly in

521   Greenland (~2.4%) and decreases elsewhere due to our downscaling procedure (Section 5.2),

522 we propose that the differences in bulk ice runoff are mostly inherent to our MAR inputs. In

523 fact, downscaling brought our dataset more in-line with non-Greenland ice runoff products

524 of Bamber et al. (2018).

525
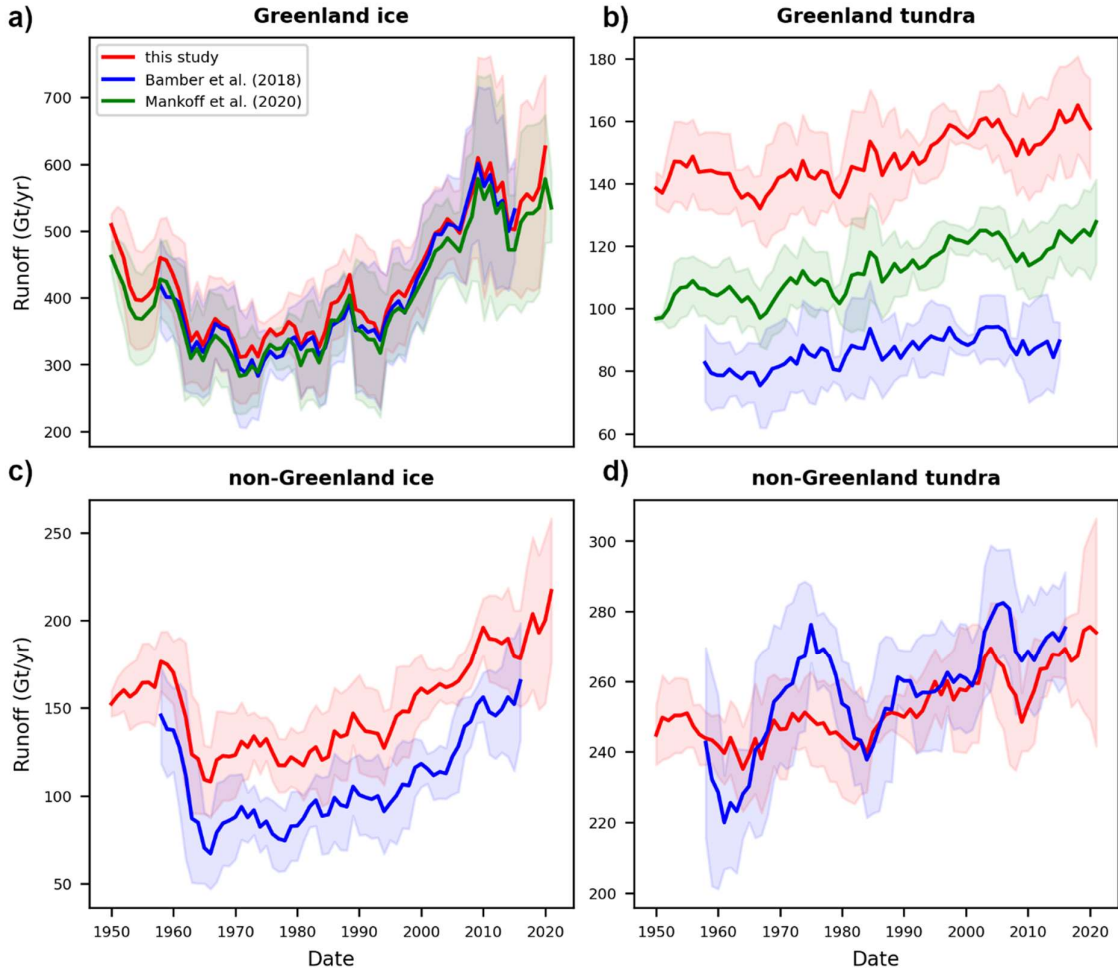
Figure 10. Bulk ice and land/tundra runoff for Greenland and all other Arctic regions, except
the Russian Arctic. Graphs show the 5-year running means, while shaded areas show the 5-
year running standard deviation. Note that Greenland ice includes PGIC.

529 The offset between land/tundra runoff estimates from the three datasets for

530 Greenland is larger than for ice runoff – with the 1σ intervals largely not overlapping – though

531 the trends and variability are very similar (Figure 10b). The mean difference between our bulk

532 land runoff and that of Bamber et al. (2018) and Mankoff et al. (2020) is +61.5 Gt and +36.1

533 Gt (+72.7% and +32.5%), respectively. Although alignment of the trends and variability of

534 tundra runoff estimations outside of Greenland is relatively poor, especially before 1980,

535 runoff magnitudes are similar without a clear pattern of over- or underestimation (Figure

536 10d). The mean difference between our product and the Bamber et al. (2018) dataset is -5.6

537   Gt (-1.7%), while the Root Mean Squared Deviation is 16 Gt. We believe the relatively poor

538   alignment of our non-Greenland tundra runoff pre-1980 with the Bamber et al. (2018) dataset

539   is related to their use of different RACMO versions in Greenland and the rest of the Arctic

540   (2.3p2 and 2.3p1 respectively) and the two sources of re-analysis forcings, ERA40 (1958-1978)

541   and ERA-Interim (1979-2016). Bulk tundra runoff increases everywhere in the Arctic due to

542   our downscaling procedure (Section 5.2). However, this increase is moderate in Greenland

543   (7.3 %), so only a fraction of the observed bulk runoff difference can be attributed to

544   downscaling. For non-Greenland tundra, where bulk runoff from the two products is similar

545   in magnitude, downscaling reduced inherent differences.

546   In conclusion, we propose that differences between our bulk ice and land runoff

547   results and the corresponding products by Bamber et al. (2018) and Mankoff et al. (2020), are

548   mostly inherent to our MAR inputs. As the three datasets differ substantially, it is difficult to

549   precisely explain the source of these inherent differences, however, different RCMs (MAR vs.

550   RACMO), different model versions (MAR 3.11 vs. MAR 3.11.5), different static and dynamic

551   (e.g. re-analysis) RCM forcings could be the most important factors. Our downscaling

552   procedure only played a secondary role, by reinforcing inherent differences in Greenland and

553   dampening them elsewhere. The exact reasons behind this warrant further study.

554   **6. Sources of uncertainty**

555   Uncertainties have affected our products at various stages of processing. Firstly,

556   MAR products have introduced a degree of uncertainty into our results due to the physical

557   simplifications of the MAR model (e.g. Fettweis, 2020). Although MAR does not provide

558   formal spatiotemporally varying uncertainty products; based on analysis from the Greenland

559   Surface Mass Balance Intercomparison Project (GrSMBIP), its overall runoff uncertainty is

560   approximately ±15% (Fettweis et al., 2020).

561   The statistical downscaling procedure – which includes corrections applied to the

562   low-resolution MAR ice and land masks – has also introduced uncertainty into our runoff

563   products. Formal uncertainty that is specific to runoff downscaling is difficult to obtain as

564   localised in-situ runoff measurements are extremely hard to obtain in the field. Given this

565   limitation, previous investigations evaluated downscaled SMB estimations against SMB

566   measurements, which are easier to obtain in the field, and found that downscaling reduced

567 the RMSE by 9-24% in the ablation zone (Noël et al., 2016; Tedesco et al., 2023). Although,

568 these results are not directly applicable to our study – as they refer to SMB, used different

569 data sources, and applied downscaling techniques that are somewhat different – they

570 indicate that elevation dependent downscaling can improve data quality. This, together with

571 the validation and comparison exercises we carried out (Section 5), suggest that the

572 uncertainty profile of our dataset is similar to previous products (e.g. Mankoff et al. (2020).

573 We, therefore, consider our product an improvement in terms of spatial coverage (compared

574 to Mankoff et al., 2020) and resolution (compared to Bamber et al., 2018), but not predictive

575 performance which remains in-line with previous products.

576   The final, coastal meltwater discharge product also has uncertainties due to the

577 simplified hydrological routing procedure. The first of these is caused by the assumption that

578 meltwater is routed on the surface. Meltwater can, and usually does, enter the englacial and

579 subglacial drainage system, where it follows a different hydraulic head. However, it is

580 complicated to quantify the location, timing and magnitude of subglacial capture, and the

581 exact path this meltwater follows. Therefore, it is difficult to ascertain which approach

582 introduces a larger uncertainty, using surface or subglacial routing exclusively. We have

583 mitigated this uncertainty by providing meltwater discharge only at the coastlines. This

584 implicitly carries out spatial averaging in areas where hydrological routing is only affected by

585 the surface hydraulic head, i.e. the location and magnitude of meltwater discharge at the ice-

586 land interface can be heavily affected by subglacial routing but this effect is weaker

587 downstream. However, this approach cannot mitigate uncertainty in ice-ocean discharge,

588 thus our product is less reliable at these interfaces.

589   The hydrological routing and the runoff integration procedure, has also assumed that

590 meltwater is instantaneously transported to the discharge point on the coastline. Besides the

591 actual transport time of meltwater within their conduits, which is affected by a complex array

592 of factors, many mechanisms can lead to meltwater retention and buffering (Forster et al.,

593 2014, Ran et al., 2024). MAR includes an approximation for retention and release of

594 meltwater in the firn layer, and a time delay for bare ice runoff (Fettweis et al., 2013, 2017;

595 Maure et al., 2023), though these are expected to be highly uncertain. Retention, storage,

596 and release of meltwater in the surface- (e.g. in supraglacial ponds, terrestrial lakes and

597 regolith), englacial/subglacial- (e.g.: in moulins, subglacial lakes, cavities, and sediment), and

598 proglacial hydrological system (e.g.: frontal and lateral lakes, lakes on the tundra,

599 groundwater) are completely unaccounted for. E.g. the duration of buffered meltwater
600 storage in the Greenland Ice Sheet can range between 4 and 9 weeks (Ran et al., 2024). Thus,
601 a significant delay can occur between melting and discharge at the coastal outflow point.
602 These factors introduce uncertainty into the estimated discharge volume time-series at the
603 coastlines.

604 **6. Code and data availability**

605 Data are available at https://doi.pangaea.de/10.1594/PANGAEA.967544 (Igneczi
606 and Bamber, 2024). Code is available at:
607 https://github.com/ignecziadam/meltwater_discharge.git

608 **Competing interests**

609 The contact author has declared that none of the authors has any competing interests

610 **Acknowledgements**

611 This work was funded by the European Union's Horizon 2020 research and
612 innovation programme through the project Arctic PASSION (grant number: 101003472). We
613 also thank X. Fettweis for providing MAR outputs. JLB was also funded by the German Federal
614 Ministry of Education and Research (BMBF) in the framework of the international future AI
615 lab "AI4EO -- Artificial Intelligence for Earth Observation: Reasoning, Uncertainties, Ethics and
616 Beyond" (grant number: 01DD20001).

References

Bamber, J. L., Tedstone, A. J., King, M. D., Howat I. M., Enderlin, E. M., van den Broeke, M. R., Noël, B.: Land ice freshwater budget of the Arctic and North Atlantic Oceans: 1. Data, Methods, and Results, Journal of Geophysical Research: Oceans, 123, 1827-1837, https://doi.org/10.1002/2017JC013605, 2018.

Biastoch, A., Schwarzkopf, F. U., Getzlaff, K., Rühs, S., Martin, T., Scheinert, M., Schulzki, T., Handmann, P., Hummels, R., Böning, C. W.: Regional imprints of changes in the Atlantic Meridional Overturning Circulation in the eddy-rich ocean model VIKING20X, Ocean Science, 17, 117-1211, https://doi.org/10.5194/os-17-1177-2021, 2021.

Böning, C. W., Behrens, E., Biastoch, A., Getzlaff, K., Bamber J. L.: Emerging impact of Greenland meltwater on deepwater formation in the North Atlantic Ocean, Nature Geoscience, 9, https://doi.org/10.1038/NGEO2740, 2016.

Ciracì, E., Veliconga, I., Swenson, S.: Continuity of the mass loss of the world's glaciers and ice caps from the GRACE and GRACE Follow-on missions, Geophysical Research Letters, 47 (9), https://doi.org/10.1029/2019GL086926, 2020.

Cowton, T. R., Todd, J. A., Benn, D. I.: Sensitivity of tidewater glaciers to submarine melting governed by plume locations, Geophysical Research Letters, 46 (11), 11219-11227, https://doi.org/10.1029/2019GL084215, 2019.

Das, S. B., Joughin, I., Benn, M., Howat, I., King, M., Lizarralde, D., Bhatia, M.P.: Fracture propagation to the base of the Greenland Ice Sheet during supraglacial lake drainage. Science 320, 963–964, https://doi.org/10.1126/science.1153360, 2008.

Davison, B.J., Sole, A.J., Livingstone, S.J., Cowton, T.R., Nienow, P.W.: The influence of hydrology on the dynamics of land-terminating sectors of the Greenland Ice Sheet, Frontiers in Earth Science, 7, https://doi.org/10.3389/feart.2019.00010, 2019.

Delmotte, Zhai, V. P., Pirani, A., Connors, S. L., Péan, C., Berger, S., Caud, N., Chen, Y., Goldfarb, L., Gomis, M. I., Huang, M., Leitzell, K., Lonnoy, E., Matthews, J. B. R., Maycook, T. K., Waterfield, T., Yelekçi, O., Yu, R., Zhou, B. (eds.)]. Cambridge university Press, Cambridge, united Kingdom and New York, NY, USA, https://doi.org/10.1017/9781009157896, 2021.

Dukhovskoy, D. S., Yashayaev, I., Proshutinsky, A., Bamber J. L., Bashmachnikov, I. L., Chassignet, E. P., Lee, C. M., Tedstone, A. J.: Role of Greenland freshwater anomaly in the recent freshening of the Subpolar North Atlantic, Journal of Geophysical Research: Oceans, 124, 3333-3360, https://doi.org/10.1029/2018JC014686, 2019.

Dutra, E., Muñoz-Sabater, J., Boussetta, S. , Komori, T., Hirahara, S., Balsamo, G.: Environmental Lapse Rate for High-Resolution Land Surface Downscaling: An Application to ERA5, Earth and Space Science, 7 (5), https://doi.org/10.1029/2019EA000984, 2020.

Enderlin, E. M., Howat, I. M., Jeong, S., Noh, M. J., van Angelen, J. H., can den Broeke, M. R.: An improved mass budget for the Greenland Ice Sheet, Geophysical Research Letters, 41 (3), 866-872. https://doi.org/10.1002/2013GL059010, 2014.

ESA: Copernicus GLO-90 DEM DGED, https://doi.org/10.5270/ESA-c5d3d65 [Date Accessed: 16/10/2022], 2021.

Fettweis, X., Franco, B., Tedesco, M., van Angelen, J.H., Lenaerts, J.T.M., van den Broeke, M.R., Gallée, H.: Estimating the Greenland ice sheet surface mass balance contribution to

659   future sea level rise using the regional atmospheric climate model MAR, The Cryosphere, 7,
660   469-489, https://doi.org/10.5194/tc-7-469-2013, 2013.

661   Fettweis, X., Box, J.E., Agosta, C., Amory, C., Kittel, C., Lang, C., van As, D., Machguth, H.,
662   Gallée, H.: Reconstructions of the 1900-2015 Greenland ice sheet surface mass balance
663   using the regional MAR model, The Cryosphere, 11, 1015-1033, https://doi.org/10.5194/tc-
664   11-1015-2017, 2017.

665   Fettweis, X., et al..: GrSMBMIP: intercomparison of the modelled 1980–2012 surface mass
666   balance over the Greenland Ice Sheet, The Cryosphere, 14, 3935–3958,
667   https://doi.org/10.5194/tc-14-3935-2020, 2020.

668   Forster, R. R., Box, J. E., van den Broeke, M., Miège, C., Burgess, E. W., van Angelen, J. H.,
669   Lenaerts, J. T. M., Koenig, L. S., Paden, J., Lewis, C., Gogieni, S. P., Leuschen, C., McConnel, J.
670   R.: Extensive liquid meltwater storage in firn within the Greenland ice sheet, Nature
671   Geoscience, 7, 95-98, https://doi.org/10.1038/ngeo2043, 2014.

672   Franco, B., Fettweis, X., Lang, C., Erpicum, M.: Impact of spatial resolution on the modelling
673   of Greenland Ice Sheet surface mass balance between 1990-2010, using the regional climate
674   model MAR, The Cryosphere, 6, 695-711, https://doi.org/10.5194/tc-6-695-2012, 2012

675   Frederikse, T., Landerer, F., Caron, L., Adhikari, S., Parkes, D., Humprey, V. W., Dangendorf,
676   S., Hogarth, P., Zanna, L., Cheng, L., Wu, Y. H.: The causes of sea-level rise since 1900,
677   Nature, 584, 393-397, https://doi.org/10.1038/s41586-020-2591-3, 2020.

678   Gao, L., M. Bernhardt, and K. Schulz, "Elevation correction of ERA-Interim temperature data
679   in complex terrain," Hydrology and Earth System Sciences, 16(12), 4661–4673,
680   https://doi.org/10.5194/hess-16-4661-2012, 2012.

681   Gao, L., Bernhardt, M., Schulz, K., Chen, X.: Elevation correction of ERA-Interim temperature
682   data in the Tibetan Plateau, International Journal of Climatology, 37(9), 3540–3552,
683   https://doi.org/10.1002/JOC.4935, 2017.

684   Gillard, L. C., Hu, X., Myers, P. G., Bamber, J. L.: Meltwater pathways from marine
685   terminating glaciers of the Greenland Ice Sheet, Geophysical Research Letters, 43, 10873-
686   10882, https://doi.org/10.1002/2016GL070969, 2016.

687   Hanna, E., Huybrechts, P., Janssens, I., Cappelen, J., Steffen, K., and Stephens, A.: Runoff and
688   mass balance of the Greenland ice sheet: 1958–2003, Journal of Geophysical Research -
689   Atmosphere, 110, https://doi.org/10.1029/2004JD005641, 2005

690   Hanna et al., E., Huybrechts, P., Steffen, K., Cappelen, J., Huff, R., Shuman, C., Irvine-Fynn, T.,
691   Wise, S., Griffiths, M.: Increased runoff from melt from the Greenland Ice Sheet: a response
692   to global warming, Journal of Climate, 21(2), 331–341,
693   https://doi.org/10.1175/2007JCLI1964.1, 2008.

694   Hanna, E., Huybrechts, P., Cappelen, J., Steffen, K., Bales, R. C., Burgess, E., McConnell, J. R.,
695   Steffensen, J. P., Van den Broeke, M., Wake, L., Bigg, B., Griffiths, M., Savas, D.: Greenland
696   Ice Sheet surface mass balance 1870 to 2010 based on Twentieth Century Reanalysis, and
697   links with global climate forcing, Journal of Geophysical Research -Atmosphere, 116,
698   https://doi.org/10.1029/2011JD016387, 2011

Hawkings, J., Wadham, J., Telling, J., Bagshaw, E., Beaton, A., Chandler, D., Dubnick, A.: Proglacial discharge measurements, Kiattuut Sermiat glacier, south Greenland (near Narsarsuaq), Zenodo, https://doi.org/10.5281/zenodo.3685976, 2016a.

Hawkings, J., Wadham, J., Tranter, M., Telling, J., Bagshaw, E.,Beaton, A., Simmons, S.-L., Chandler, D., Tedstone, A., and Nienow, P.: The Greenland Ice Sheet as a hot spot of phosphorus weathering and export in the Arctic, Global Biogeochemical Cycles, 30(2), 191–210, https://doi.org/10.1002/2015gb005237, 2016b.

Howat, I.: MEaSUREs Greenland Ice Mapping Project (GIMP) Land Ice and Ocean Classification Mask, Version 1 [GimpIceMask_90m_2015_v1.2]. Boulder, Colorado USA. NASA National Snow and Ice Data Center Distributed Active Archive Center. https://doi.org/10.5067/B8X58MQBFUPA [Date Accessed: 16/10/2022], 2017.

Howat, I.M., A. Negrete, B.E. Smith: The Greenland Ice Mapping Project (GIMP) land classification and surface elevation datasets, The Cryosphere, 8, 1509-1518, doi:10.5194/tc-8-1509-2014, 2014.

Hugonnet, R., McNabb R., Berthier E., Menounos B., Nuth, C., Girod, L., Farinotti, D., Huss, M., Dussaillant, I., Brun, F., Kääb, A.: Accelerated global glacier mass loss in the early twenty-first century, Nature, 592, 726-731, https://doi.org/10.1038/s41586-021-03436-z, 2021.

Igneczi, A., Bamber, J. L.: Pan-Arctic land-ice and tundra meltwater discharge database from 1950 to 2021, PANGAEA, https://doi.org/10.1594/PANGAEA.967544, 2024.

Ignéczi, Á., Sole, A., Livingstone, S., Ng, F., Yang, K.: Greenland Ice Sheet surface topography and drainage structure controlled by the transfer of basal variability, Frontiers in Earth Science, 6(101), https://doi.org/10.3389/feart.2018.00101, 2018.

IPCC: Climate Change 2021: The Physical Science Basis. Contribution of Working Group I to the Sixth Assessment Report of the Intergovernmental Panel on Climate Change [Masson-Delmotte, V., P., Zhai, A., Pirani, S. L., Connors, C., Péan, S., Berger, N., Caud, Y., Chen, L., Goldfarb, M. I., Gomis, M., Huang, K., Leitzell, E., Lonnoy, J. B. R., Matthews, T. K., Maycock, T., Waterfield, O., Yelekçi, R., Zhou, Y., Zhou, B. (eds.)]. Cambridge University Press, Cambridge, United Kingdom and New York, NY, USA, 2391 pp. doi:10.1017/9781009157896, 2021.

King, M. D., Howat, I. M., Candela, S. G., Noh, M. J., Jeong, S., Noël, B., can den Broeke, M. R., Wouters, B., Negrete, A.: Dynamic ice loss from the Greenland Ice Sheet driven by sustained glacier retreat, Communications Earth & Environment, 1, 1, https://doi.org/10.1038/s43247-020-0001-2, 2020.

Kondo, K., Sugiyama, S.: Discharge measurement at the outlet stream of Qaanaaq Glacier in the summer 2017–2019, GEUS Data Center, https://doi.org/10.22008/hokkaido/data/meltwater_discharge/qaanaaq, 2020.

Krawczynski, M., Behn, M., Das, S., and Joughin, I.: Constrains on the lake volume required for hydrofracture through ice sheets. Geophys. Res. Lett., 36:L10501. https://doi.org/10.1029/2008GL036765, 2009.

Langley, K.: GEM river discharge measurements, GEUS Data Center, https://doi.org/10.22008/asiaq/data/meltwater_discharge/gem, 2020.

740 Lu, Y., Yang, K., Lu, X., Li, Y., Gao, S., Mao, W., Li, M.: Response of supraglacial rivers and
741 lakes to ice flow and surface melt on the northeast Greenland ice sheet during the 2017
742 melt season, Journal of Hydrology, 602, https://doi.org/10.1016/j.jhydrol.2021.126750,
743 2021.

744 Mankoff, K. D., Noël, B., Fettweis, X., Ahlstrøm A. P., Colgan, W., Kondo, K., Langley, K.,
745 Sugiyama, S., van As, D., Fausto, R. S.: Greenland liquid water discharge from 1958 through
746 2019, Earth System Science Data, 12, 2811-2841, https://doi.org/10.5194/essd-12-2811-
747 2020, 2020.

748 Maure, D., Kittel, C., Lambin, C., Delhasse, A., and Fettweis, X.: Spatially heterogeneous
749 effect of the climate warming on the Arctic land ice, Cryosph. Discuss., 2023, 1–20,
750 https://doi.org/10.5194/tc-2023-7, 2023.

751 Melton, A. M., Alley, R. B., Anandakrishnan, S., Parizek, B. R., Shanin, M. G., Stearns, L. A.,
752 LeWinter, A. L., Finnegan D. C.: Meltwater drainage and iceberg calving observed in high-
753 spatiotemporal resolution at Helheim Glacier, Greenland, Journal of Glaciology, 68 (270),
754 812-828, https://doi.org/10.1017/jog.2021.141, 2022.

755 Millan, R., Mouginot, J., Rabatel, A., Morlighem, M.: Ice velocity and thickness of the world's
756 glaciers, Nature Geoscience, 15, 124-129, https://doi.org/10.1038/s41561-021-00885-z,
757 2022.

758 Morlighem, M., et al.: BedMachine v3: Complete bed topography and ocean bathymetry
759 mapping of Greenland from multi-beam echo sounding combined with mass conservation,
760 Geophysical Research Letters, 44(21), 11051-11061 https://doi.org/10.1002/2017GL074954,
761 2017.

762 Mouginot, J., Rignot, E., Bjørk A. A., van den Broeke, M., Millan, R., Morlighem, M., Noël, B.,
763 Scheuchl, B., Wood, M.: Forty-six years of Greenland Ice Sheet mass balance from 1972-
764 2018, Proceedings of the National Academy of Sciences, 116 (19), 9239-9244,
765 https://www.pnas.org/doi/full/10.1073/pnas.1904242116, 2019.

766 Noël, B., Jan van de Berg, W., Machguth, H., Lhermitte, S., Howat, I., Fettweis, X., van den
767 Broeke, M.R.: A daily, 1km resolution data set of downscaled Greenland ice sheet surface
768 mass balance (1958–2015), The Cryosphere, 10, 2361-2377, https://doi.org/10.5194/tc-10-
769 2361-2016, 2016.

770 Proshutinsky, A., Dukhovskoy, D., Timmermans, M-L., Krishfield, R., Bamber, J. L.: Arctic
771 circulation regimes, Philosophical Transactions of the Royal Sociate A, 373 (2052),
772 https://doi.org/10.1098/rsta.2014.0160, 2015.

773 Ran, J., Ditmar, P., van den Broeke, M. R., Liu, L., Klees, R., Khan, S. A., Moon, T., Li, J., Bevis,
774 M., Zhong, M., Fettweis, X., Liu, J., Noël, B., Shum, C. K., Chen, J., Jiang, L., van Dam, T.:
775 Vertical bedrock shifts reveal summer water storage in Greenland ice sheet, Nature, 635,
776 108-113, https://doi.org/10.1038/s41586-024-08096-3, 2024.

777 Rantanen, M., Karpechko, A. Y., Lipponen, A., Nordling, K., Hyvärinen, O., Rousteenoja, K.,
778 Vihma, T., Laaksonen, A.: The Arctic has warmed nearly four times faster than the globe
779 since 1979, Communications Earth & Environment, 3, 168, https://doi.org/10.1038/s43247-
780 022-00498-3, 2022.

781 Ryan, J. C., Smith, L. C., van As, D., Cooley, S. W., Cooper, M. G., Pitcher, L. H., Hubbard, A.:
782 Greenland Ice Sheet surface melt amplified by snowline migration and bare ice exposure,
783 Science Advances, 5(3), https://doi.org/10.1126/sciadv.aav3738, 2019.

784 RGI Consortium: Randolph Glacier Inventory – A dataset of global glacier outlines, Version 6,
785 Boulder, Colorado, USA, NSIDC: National Snow and Ice Data Center,
786 https://doi.org/10.7265/4m1f-gd79 [Date Accessed 17/10/2022], 2017.

787 Smith, B., Fricker, H. A., Gardner, A. S., Medley, B., Nilsson, J., Paolo, F. S., Holschuh, N.,
788 Adusumili, S., Brunt, K., Csatho, B., Harbeck, K., Markus, T., Neumann, T., Siegfried, M. R.,
789 Zwally, H. J.: Pervasive ice sheet mass loss reflects competing ocean and atmosphere
790 processes, Science, 368, 1239-1242, https://doi.org/10.1126/science.aaz5845, 2020.

791 Snyder, J. P.: Map projections–A working manual. Washington, DC: USGPO, 1987.

792 Sugiyama, S., Sakakibara, D., Matsuno, S., Yamaguchi, S., Matoba, S., and Aoki, T.: Initial field
793 observations on Qaanaaq ice cap, northwestern Greenland, Annals of Glaciology, 55, 25–33,
794 https://doi.org/10.3189/2014aog66a102, 2014.

795 Tedesco, M., Colosio, P., Fettweis, X., Cervone, G.: A computationally efficient statistically
796 downscaled 100 m resolution Greenland product from the regional climate model MAR, The
797 Crysophere, 17, 5061-5074, https://doi.org/10.5194/tc-17-5061-2023, 2023.

798 Tepes, P., Gourmelen, N., Nienow, P., Tsamados, M., Shepherd, A., Weissgerber, F.: Changes
799 in elevation and mass of Arctic glaciers and ice caps, 2010-2017, Remote Sensing of
800 Environment, 261, https://doi.org/10.1016/j.rse.2021.112481, 2021.

801 van As, D., Hasholt, B., Ahlstrøm, A. P., Box, J. E., Cappelen, J., Colgan,W., Fausto, R. S.,
802 Mernild, S. H., Mikkelsen, A. B., Noël, B. P. Y., Petersen, D., van den Broeke, M. R.:
803 Reconstructing Greenland Ice Sheet meltwater discharge through the Watson River (1949–
804 2017), Arctic Antarctic and Alpine Research, 50, S100010.
805 https://doi.org/10.1080/15230430.2018.1433799, 2018.

806 Van den Broeke, M. R., Enderlin, E. M., Howat, I. M., Munneke, P. K., Noël, B., van de Berg,
807 W. J., van Meijgaard, E., Wouters, B.: On the recent contribution of the Greenland Ice Sheet
808 to sea level change, The Cryosphere, 10, 1933-1946, https://doi.org/10.5194/tc-10-1933-
809 2016, 2016.

810 Yang, Q., Dixon, T. H., Myers, P. G., Bonin, J., Chambers, D., van den Broeke, M. R.,
811 Ribergaard, M. H., Mortensen, J.: Recent increases in Arctic freshwater flux affects Labrador
812 Sea convection and Atlantic overturning circulation, Nature Communications, 7,
813 https://doi.org/10.1038/ncomms10525, 2016.

814 Yang, K., Smit, L.C., Sole, A., Livingstone, S.J., Cheng, X., Chen, Z., Li, M.: Supraglacial rivers
815 on the northwest Greenland Ice Sheet, Devon Ice Cap, and Barnes Ice Cap mapped using
816 Sentinel-2 imagery, International Journal of Applied Earth Observation and Geoinformation,
817 78, 1-13, https://doi.org/10.1016/j.jag.2019.01.008, 2019.

818 Zhang, W., Yang, K., Smith, L.C., Wang Y., van As, D., Noël, B., Lu, Y., Liu, J.: Pan-Greenland
819 mapping of supraglacial rivers, lakes, and water-filled crevasses in a cool summer (2018) and
820 a warm summer (2019), Remote Sensing of the Environment, 297,
821 https://doi.org/10.1016/j.rse.2023.113781, 2023.